

Image-based Reconstruction of Tissue Scatterers using Beam Steering for Ultrasound Simulation

Oliver Mattausch, *Member, IEEE*, and Orcun Goksel, *Senior Member, IEEE*

Abstract—Numerical simulation of ultrasound images can facilitate the training of sonographers. An efficient and realistic model for the simulation of ultrasonic speckle is the convolution of the ultrasound point-spread function with a distribution of point scatterers. Nevertheless, for a given arbitrary tissue type, a scatterer map that would generate a realistic appearance of that tissue is not known a priori. In this paper, we introduce a principled approach to estimate (reconstruct) such a scatterer map from images, by solving the inverse-problem of ultrasound speckle formation, such that images from arbitrary view angles and transducer settings can be generated from those scatterer maps later in simulations. Robust reconstructions are achieved by using multiple measurements of the same tissue with different viewing parameters. For this purpose, a novel use of beam-steering to rapidly and conveniently acquire multiple images of the same scene is proposed. We demonstrate in numerical and physical phantoms and *in vivo* images that the appearance of synthesized images closely match real images for a range of viewing parameters and probe settings. We also present a scene editing scenario exploiting these scatterer representations to create realistic images of augmented anatomy.

I. INTRODUCTION

Ultrasound (US) simulation is essential in the context of virtual-reality training of medical students and personnel. Ultrasound is a radiation-free, low-cost, and real-time medical imaging modality, and hence it is commonly used in clinical examinations. However, its low signal-to-noise ratio and the existence of various ultrasound-specific artifacts necessitate extensive training of sonographers for performing a particular ultrasound examination technique and/or the imaging of a specific organ. Current standard education is in the form of imaging plastic phantoms and mannequins, as well as supervised examination of real pathology from patients during clinical practice. The former are not sufficiently realistic, and the latter requires additional time investment of both qualified personnel (the supervisor) and the patient, as well as potentially compromising the medical service the patient receives. With the above, another challenge is the training of rare pathologies. Reis et al. [30] reports that during one year of standard education the medical students have a chance to learn only 80% of the important pathologies. For example, assuming that approximately 100 pregnancies are attended by an obstetrics and gynecology expert a year, heart-failure (a

relatively common condition) will be observed on average once a year, whereas skeletal malformation (a rare 1/5000 condition) may take 50 years to encounter – longer than the typical career of an obstetrician. These rare pathologies are still of utmost importance to identify, arguably even more so than common cases; and with such low occurrence rates their training on actual patients becomes unlikely. Other common decisions judged from US imaging can also be quite crucial, such as the assessment of embryonic gestational age in the face of a possible abortion; thus, a standardized training of sonographers is highly desired. These indicate the need for computer-based training of ultrasound examinations, where different anatomical scenes and pathologies shall be simulated in a virtual-reality environment *realistically* and in *real-time*.

Interpolative methods use pre-recorded patient data, through which an ultrasound plane can be sliced in simulation time without [1] or with [11] tissue deformation taken into account. Despite yielding photo-realistic images, this constrains the simulations drastically by only allowing simulation at voxels where data is available and also limiting image settings and viewing angles to those used in the acquisition. *Wave-based* simulation, such as FieldII [17], is an alternative that is accurate but slow and thus typically used only for offline simulation. *Ray-based methods* [6], [22], [23], [42] are suitable for interactive US generation and can successfully model ultrasound interactions with large-scale structures. However, they are less suited for simulating sub-wavelength interactions, at the scale of which wave-like properties become predominant and create the typical noise patterns known as ultrasonic speckle. These are caused by the interference of scattered echoes from countless microscopic structures in the tissue, commonly called *scatterers*.

For given scatterers, convolution techniques can generate ultrasound images with realistic speckle patterns [4], [10]. However, a scatterer representation of an anatomical volume is often not readily available. Therefore, in convolution-based simulations (e.g., FieldII and ray-based methods [6], [23]) scatterers are typically created as statistical distributions of continuous spatial variables [17], [25]. Then, the problem becomes how to tune a suitable parametrization for generating a particular tissue type. One approach is the tedious process of manual trial-and-error by observing generated images, but this would quickly become infeasible, since the final appearance relates to scatterer distribution in a non-trivial fashion [28]. Due to above complexities, images simulated with these techniques often appear artificial and toy-like [17]. For instance, a sample fetus image modeled and simulated using the scatterer parametrization of [6] is shown in Fig. 1, which looks still artificial despite a considerable amount of manual effort [23]

Manuscript received Feb 1, 2017; revised Sep 8, 2017; accepted Oct 23, 2017. This work was supported by the Swiss Commission for Technology and Innovation (CTI) and the Swiss National Science Foundation (SNSF).

O. Mattausch and O. Goksel are with the Computer-assisted Applications in Medicine Group, Computer Vision Lab, ETH Zurich, Switzerland.

Copyright (c) 2017 IEEE. Personal use of this material is permitted. However, permission to use this material for any other purposes must be obtained from the IEEE by sending a request to pubs-permissions@ieee.org.

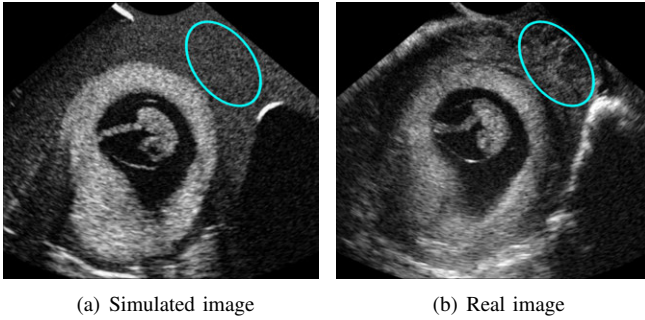


Fig. 1. Interactive simulation (a) and real image (b) of a fetus. Simulated ultrasound tissue created by hand (e.g., using parametrization [6]) are often too toy-like to convince specialists in virtual training simulations [23] and miss the complexities of actual tissue (see marked tissues). Our method automatically creates realistic tissue models for such simulations.

for parameterizing scatterer distributions aiming for realism.

We propose herein to extract scatterer maps and patterns from example images. This can be used to approximate an underlying scatterer representation that would create the observed image, when given as input to a convolution-based simulation, but also allowing to alter imaging frequency, probe geometry, viewing direction, and others in such simulation process. Speckles in the image-space are then transformed into a scatterer representation as a physical-space representation of the imaged anatomy. Furthermore, distributions and parametric representations can be extracted and learned from such scatterer instances, e.g., to model a particular tissue type from given image samples.

In our previous work [20], preliminary results of an inverse method for estimating scatterers were presented. Therein single images were used for estimations, which is hereby shown to yield suboptimal scatterer reconstructions that are not robust to change of viewing parameters. Furthermore, such parametrizations often lack the visual variety of real tissue, such as micro-vasculature, muscle fibers, fat streaks, micro-calcifications, and other imperfections.

Alessandrini et al. [2] proposed a pipeline for the simulation of synthetic echocardiographic sequences. For this, an image region is populated with randomly-placed points, the amplitudes of which are set using B-mode images after removing the effect of logarithmic-compression using an inverse-log scaling. These points form a non-Cartesian interpolation grid, which can then be relocated, e.g., for animating deformation. An image is subsequently simulated using the fast convolution algorithm COLE [10]. This method was shown to provide visually pleasing echocardiographic images by the authors [2], and is similar to ours in that point amplitudes are obtained from sample ultrasound images. However, these interpolation points are not ultrasound scatterers as defined in our and earlier models, as the actual complex-valued (e.g., cosine modulated) PSF is not considered and the extraction is performed from scaled B-mode (pseudo-envelope) images, which do not contain the RF phase information. This prohibits, for instance, the modeling of (destructive) interference between scatterers, and thus its simulation afterward.

We propose an inverse-problem approach to reconstruct scatterers based on speckle observations, such that plausible

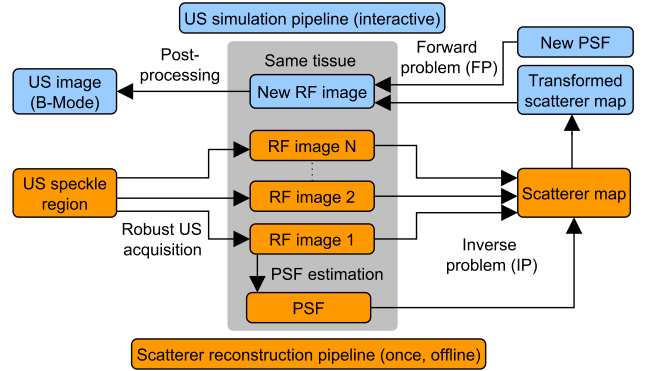


Fig. 2. Problem definition. From one or many input images of the same region of ultrasonic speckle, a map of scatterers is created by solving an inverse problem (in orange, from left to right). Such scatterer map is for simulation of new images of the same tissue with different imaging parameters (in blue, from right to left).

images of this tissue region can be generated in simulations. An overview of our method is shown in Fig. 2, where the orange color refers to the inverse problem, and blue to the forward problem of ultrasound simulation. Electronic beam steering is used to acquire several ultrasound images of a tissue region as raw beamformed radio-frequency (RF) data, using a single input image to estimate the ultrasonic point-spread function (PSF). Given this PSF and RF images, a deconvolution inverse-problem can be setup to find a scatterer realization *robustly*, due to the multiplicity of input images.

These scatterers can later be used directly or in a modified form, with the original or an altered PSF, to generate new simulated images of this tissue region. This is achieved by using ultrasound convolution of the scatterers with the PSF to obtain a new RF image, which is finally converted to a typical B-mode image after post-processing.

Our problem setup has similarities with blind deconvolution methods [7], [26]. However, unlike these methods our goal is not the true-to-real *restoration* of blurry US images. Instead, we aim to find a scatterer representation that can be used to *realistically synthesize new US images under potentially-different viewing conditions*; e.g., from a different viewing direction as shown in Fig. 3 (a) or at a different imaging frequency. Accordingly, we propose a robust reconstruction method by means of constrained regularized optimization using the ℓ_1 -norm. To achieve robustness with respect to varying view directions, we propose to use multiple input images. Since the precise acquisition of linearly-independent image observations can be difficult using external mechanical setups or position tracking, a novel use of electronic US beam-steering is introduced.

II. BACKGROUND

Forward problem (FP) of speckle formation. We assume a well-established convolution model of ultrasound speckle and its simulation [4], [25]. This model is presented below in 2D (ignoring the finite ultrasound beam-thickness), nevertheless, it could extend to 3D without loss of generality [10]. In

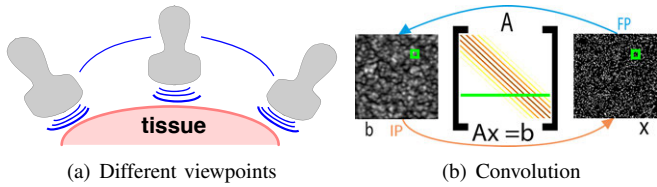


Fig. 3. (a) Multiple viewing directions in typical ultrasound examinations, often to avoid or to leverage US-specific artifacts such as shadowing and enhancement. During simulation, simply rotating images would not generate correct speckle appearance; therefore, manipulation in a physical-space is needed. (b) Forward and inverse problem of speckle formation, to reconstruct a physical representation of tissue scattering.

this model, ultrasonic speckle intensity $I(l, a)$ is obtained by convolving point-like scatterers $g(l, a)$ in the tissue with the ultrasonic impulse response $h(l, a)$, also called the point-spread function (PSF), i.e.:

$$I(l, a) = g(l, a) * h(l, a) + \gamma(l, a). \quad (1)$$

$\gamma(l, a)$ is an additive random noise term. (l, a) is the lateral and axial position with respect to the probe origin (cf. Fig. 4(a)). Alternatively, for a convex probe, the position can be represented in polar coordinates with angle l and radius a .

In a typical US transmit-receive imaging sequence with in-plane focusing, the PSF $h(l, a)$ can be approximated as a cosine modulated Gaussian pulse [6], i.e., $h(l, a) \approx e^{-\frac{l^2}{2\sigma_l^2} - \frac{a^2}{2\sigma_a^2}} \cos(2\pi fa)$. f represents the imaging center frequency, and σ_l and σ_a are the spreads of the Gaussian pulse in corresponding directions. Note that in Eq. (1), h can change locally and hence both σ 's can themselves be a function of a and l . In this work, we consider PSF changes based on the axial distance a from the transducer due to focusing, aperture, transducer geometry, etc, while ignoring lateral PSF changes, similarly to earlier simulation works [6], [23]. The PSF corresponding to a given axial image depth is denoted as h_a and can be determined empirically from observations (e.g., by imaging wires in degassed water) [32] or from acoustic simulations, e.g., using Field II [27].

In this work, we used a Field II-simulated PSF for the computer phantom results. For the *in vivo* results, the PSF was derived directly from input image observations as follows.

PSF Estimation. A number of methods exist that estimate PSF from input US images based on *homomorphic filtering* in the cepstrum domain, for the purpose of blind deconvolution of ultrasound [36] in 1-3 dimensions [18], [19], [37], [38]. These methods can be differentiated by their strategies to solve the difficult phase unwrapping problem [36], which is highly sensitive to noise in 2 or 3 dimensions [37]. In this work, we use a cepstrum-based PSF estimation method that computes local smoothly-varying PSF h_a [21], avoiding the phase-wrapping problem in 2D by assuming the PSF to be *separable* in the lateral and axial components. Homomorphic filtering [36] is a signal processing technique for decoupling signals h and g in Eq. 1 into its components in Fourier domain, i.e., $\log(\mathcal{F}(h * g)) = \log(H \cdot G) = \log H + \log G$. \mathcal{F} denotes the Fourier transform and the capitals represent Fourier transforms of signals. It basically converts the image to the cepstrum

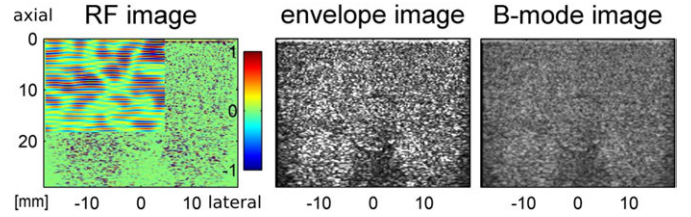


Fig. 4. Time-gain compensated RF image (left) is the input to our method. The envelope of the signal (magnitude of Hilbert transform) and the dynamic-range (log) compressed *B-mode* versions are also presented above.

domain, where the convolution becomes a linear combination (addition). Since the PSF component would change much slower compared to the image content, low-pass filtering in the cepstrum coefficients then yields the PSF. To gain robustness, we solve all points at the same depth (with expectedly similar PSF) simultaneously, and accordingly obtain a single PSF estimation h_a at that given depth – which are further regularized to be smooth in the axial direction [21].

Scatterers $g(l, a)$ are traditionally modeled with varying amplitudes and spatial positions [17], [39]. Alternatively, a discretized version of Eq. (1) can be used, e.g., for the purpose of fast GPU-based convolution [6], [23]. With this, a discrete tissue representation $g[l, a]$ is convolved with a discrete PSF $h[l, a]$, yielding sparse speckle image intensities $I[l, a]$.

Inverse problem (IP) of scatterer reconstruction. To solve the inverse problem of finding a tissue representation $g[l, a]$ for given intensities $I[l, a]$, convolution in a discretized Eq. 1 is expressed as a linear system $Ax = b$. As depicted in Fig. 3 (b), A is the convolution matrix induced by h_a , x is a column vector of scatterers obtained from vectorization of $g[l, a]$, and b is the resulting column vector of image intensities $I[l, a]$.

Inverse problems have been studied extensively in the field of US image deconvolution, for the purpose of negating the *blurring* effect of the PSF in order to improve the signal-to-noise ratio of an ultrasound image. To achieve visually pleasing (smooth) results for moderately noisy input images, the Wiener filter and ℓ_2 -regularized optimization are natural choices [15], [18]. Richardson-Lucy algorithm [9] is another alternative, which optimizes the log-likelihood of a Poisson distribution of scatterers, making it more robust to noise.

Formulations based on ℓ_1 -norm have also been studied for deconvolution [13], often in the context of sparse bases for compressed US image reconstruction [7], as they are naturally suited for sparse problems. Alternatively, methods based on generalized Gaussian distributions (GGD) can be used for models based on ℓ_p -norms, converging to a uniform distribution for $p = \infty$. This can provide more flexible noise and regularization models, achieving Gaussian and Laplacian distributions as limit cases for $1 \leq p \leq 2$, as was also shown to be beneficial for ultrasound deconvolution [44] and ultrasound tissue characterization [3]. Likewise, hybrid regularization terms combine the advantages of ℓ_2 -norms and robust ℓ_1 -norms to handle outliers, most notably the Huber norm [14].

III. METHODS

We are not interested in a visually smooth image reconstruction resulting from ℓ_2 -norm objectives. Instead, we aim to find an *intrinsic* representation of the tissue, denoted here as *scatterer map*, which can be used in subsequent forward simulations (top row of Fig. 2). Our goal is hence, given an ultrasound RF image as input (e.g., see Fig. 4), to reconstruct *sparse*, point-like scatterers as a discrete approximation to the underlying continuous convolution model (Eq. 1). A scatterer map has to be sufficiently fine-grained for an accurate discretization of the continuous scatterer model. Hence, denoting n and m respectively as the dimensions of x and b , we assume that $n > m$ and that $Ax=b$ is *underdetermined*, unlike deconvolution methods where n typically equals to m . *Robustness* must be ensured despite outliers, such as due to brighter directional reflections not accounted for in the convolution model. Accordingly, we assume a Laplacian noise distribution for γ , which may also contain outliers. Based on these requirements, we use an objective based on ℓ_1 -norm regularization, which is known to yield sparse and robust solutions for underdetermined systems. Such objectives are typically of the form:

$$\hat{x} = \arg \min_x \|Ax - b\|_1 + \lambda \|x\|_1 \quad \text{s.t. } x \geq 0. \quad (2)$$

This favors sparse x with small scatterer amplitudes. The constraint ensures the physical fact that the scatterers should have positive amplitudes. Unlike the better known $\ell_2\ell_1$ LASSO formulation, we use an $\ell_1\ell_1$ formulation with an error minimization term $\|Ax - b\|_1$ in the objective. This formulation, known as RLAD (Regularized Least Absolute Deviations), has been shown to be more robust than LASSO with respect to outliers in the error distribution [40]. It is also less sensitive to small variations of the λ parameter, since both terms in the objective use the same norm. This allows us to fix λ empirically to 0.005 in all examples in this paper.

For the vector of measurements b we use raw radio-frequency (RF) data, which contains the phase information of US echoes. The result \hat{x} is then a scatterer map which generates an approximation of the input image when convolved with the given PSF. New images can be synthesized, e.g., by applying the FP with the PSF of a different transducer geometry, or by editing (augmenting) the acquired scatterer map before applying the FP, or by using the result in combination with surface models in ray-traced simulations.

A. Robust Scatterer Reconstructions

Because of the anisotropy of a typical PSF, there is no guarantee that the scatterer map computed from a single image will produce robust speckle patterns from a different (e.g., rotated) viewing angle. In fact, due to the phase component of the PSF, the scatterer map for a particular speckle image may not be unique. It was also shown [8] that a small number of periodically-placed equi-amplitude scatterers is sufficient to generate a particular speckle image. Viewed from another direction however, this minimal set of scatterers will in general not be sufficient to recreate the speckle appearance of a target tissue – an ambiguity that could lead to variations in

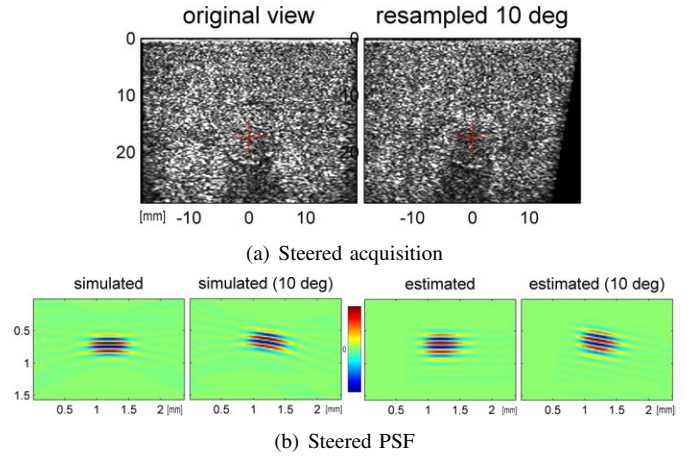


Fig. 5. (a) Acquired envelope data for 2 images steered by 0° and 10° , *scan-conversion* into physical coordinate frame. (b) Field II-simulated PSF of steered image (left), PSF estimated from said image, with steered angle approximated by rotation of 0° PSF (right).

perceived brightness and other artifacts. For a single input image this is an ill-posed problem. Thus, multiple linearly-independent measurements are used to remove any ambiguity. New measurements augment the linear system with additional rows, i.e.,

$$[A_1^\top, \dots, A_n^\top]^\top x = [b_1^\top, \dots, b_n^\top]^\top, \quad (3)$$

where A_i is the convolution matrix simulating image b_i . For such multiple observations b_i , the transducer could, e.g., be moved at tiny intervals laterally. However, this requires a difficult setup and very accurate positioning. Alternatively, we propose beam steering as a major contribution of this work in order to acquire multiple input (RF) images b_i of the same US speckle region both very quickly and accurately, requiring no hardware setup or add-on.

Electronic beam steering. Beam steering is an effective way of acquiring a sufficient number of input ultrasound images of the same region from different angles β_i (see Fig. 5(a), before and after scan conversion). More importantly, the beam steering process is sufficiently fast to minimize motion effects of the sonographer and the patient (e.g., breathing during acquisition). Note that the PSF also changes with respect to β_i and hence results in varying A_i . These PSFs can be simulated or approximated separately. In this paper, we make a small angle approximation, as a steered PSF kernel can be approximated well by a rotation of the 0° PSF kernel by β_i . For an estimated PSF, we use this fact by creating PSFs at all depths for a 0° beam and then rotating those kernels h_a individually by β to easily obtain PSF estimations for steered images. A comparison of such approximation to actual (Field II simulated) PSFs is shown in Fig. 5(b).

Canonical reference frame. Combining the steered images b_i into the same canonical reference frame, i.e., the frame corresponding to the 0° angle, effectively constitutes a more uniform and isotropic coverage of the sampling domain (see Fig. 6(a)). Note that rotated PSFs introduce lateral variance (where a 0° PSF has low lateral variance) therefore adding substantial information in resolving laterally spaced scatterers.

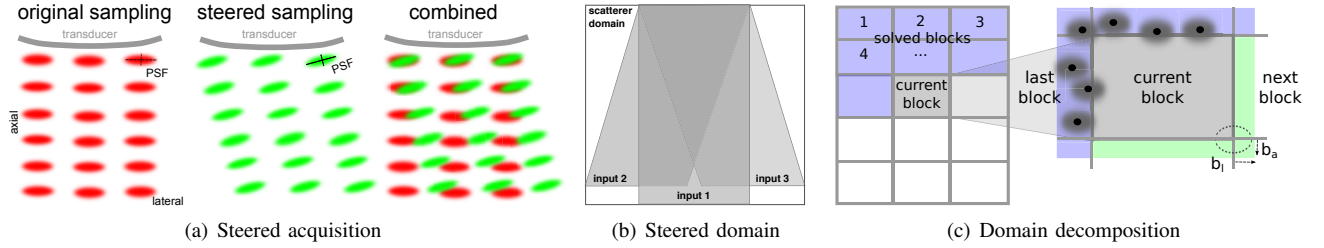


Fig. 6. The beam steering mechanics allows to electronically change the viewing angle of a probe (a) and to easily acquire multiple image observations of the same region (gray overlap) (b). Reconstructing scatterers of full image is made tractable by partitioning solution space into overlapping blocks (c).

To integrate all measurements into a single system, b_i could be transformed and scan-converted into new image measurements b'_i . However, resampling and interpolating RF lines is not a well defined operation and would introduce additional errors, and therefore is avoided in this work. Instead, we encode in A_i this transformation operation between the reference frame of measurements b_i and the canonical reference frame (and hence the space of scatterers x), which is defined by axial position a in the beam propagation axis and lateral position l centered at the transducer. Due to beam steering, the PSF h_a for a given axial position a is displaced at steering angle β by offsets δ_l and δ_a s.t.:

$$\delta_l = a \tan \beta ; \quad \delta_a = \sqrt{l^2 + a^2} - a. \quad (4)$$

δ_l and δ_a are used to displace the position of h_a on the diagonal of matrix A_i , i.e., the values of h_a are shifted downwards on each column of A_i . Fig. 5(b) depicts how multiple steered images map to the reference frame of the scatterer domain. The bounding box of all (parallelogram-shaped) steered images effectively cover a larger lateral region than a single ultrasound image, i.e., extending by the maximum lateral offset $\max(|\delta_l|)$ in each direction. Thus, the scatterer solution space is set accordingly to cover all images. In $A_i x = b_i$, the entries of A_i corresponding to parts of the solution space which are not covered by a given b_i are masked to zero. Thus, a scatterer map pixel x is affected only by an active set of images b_i , and best reconstruction results are to be expected in the center region with information from all b_i as shown by shades of gray in Fig. 6(b). Design of typical ultrasound piezoelectric crystals aim to deliver most power straight ahead and thus afford a reduced efficacy at increased steering angles, with reduced signal-to-noise ratio and hence unreliable measurements. To cope with this, we weight angle contributions such that

$$[c_1 A_1^T, \dots, c_n A_n^T]^T x = [c_1 b_1^T, \dots, c_n b_n^T]^T \quad (5)$$

where $0 \leq c_i \leq 1$ is the *confidence* in the corresponding steered observation. These weights can be obtained from transducer specifications or measured in experiments. In this work, we empirically set the weights to linearly fall-off to 0 at a horizon of β_{\max} away from the non-steered 0° direction, i.e., according to the *triangular* function $c_i = \max(0, 1 - |\beta_i|/\beta_{\max})$. We set $\beta_{\max} = 60^\circ$. Other functions such as a Gaussian falloff is conceivable, but these would have the drawback that for extreme angles where the steered images contain mostly noise, the confidence would never fall off to zero. Note that an equal contribution of all steering angles with a constant

$c_i = 1$ corresponds to $\beta_{\max} = \infty$ in the above formula. The linear system in Eq. (5) is our final problem formulation used throughout the rest of this paper.

Boundary Conditions. To explain speckle intensities near the edges of an input image b_i , a common way is to populate a margin of half the size of a PSF kernel and set boundary conditions on the domain of interest by mirroring the input data on the boundary. However, this strategy led to seams in the reconstructed images due to edges of steered images existing at many places (cf. Fig. 5(b)). Instead, we remove all rows in $A_i x = b_i$ that are not explained by actual data, assuming that scatterers in border regions are constrained by at least one of the other $A_j x = b_j$, $j \neq i$.

B. Scatterer map resolution

Since the scatterers are an abstract representation for the approximation of sub-wavelength particles, there is indeed no clear definition for their true resolution. Scatterer map resolution R_{sc} becomes important in our reconstructions, since, on the one hand, an unnecessarily fine scatterer grid leads to high complexity, increasing time and memory consumption and reducing optimization robustness/convergence. On the other hand, a very coarse grid does not allow sufficient degrees-of-freedom to represent the underlying continuum, which one can describe as uncountably-many scatterers placed at continuous spatial locations. Also, R_{sc} has to be sufficiently fine for *fully developed speckles* – a characteristics of typical speckles based on Rayleigh statistics [28].

Using the native resolution of the input RF images R_{rf} for R_{sc} , for instance, would lead to anisotropic sampling and image artifacts in the rotated frames as well as when utilizing rotated PSFs. Thus, for scatterer resolution some necessary theoretical constraints must be considered: a) From Nyquist, lateral sampling must satisfy $\Delta_a \leq \lambda_c/2$, where λ_c is the wavelength of maximum desired imaging frequency. Note that this is an upper limit, and it might practically have to be even smaller, e.g., $\lambda_c/4$. b) the sampling density should be isotropic, or $\Delta_a \approx \Delta_l$ for rotation invariance, and c) the grid resolution must be sufficiently high for the local density of scatterers to satisfy Rayleigh criterion to be able to create realistic interference patterns for arbitrary transducer angles. Since axially R_{rf} trivially satisfies (a), we choose to use this as the axial resolution of R_{sc} . For the lateral resolution, we use the nearest integer multiple of the lateral component of R_{rf} , which creates a near isotropic sampling. For a case with, e.g., 40 MHz RF sampling and a speed of sound as 1540 m/s, this

results in $\approx 20 \mu\text{m}$ in both axes in this paper, yielding 50×50 scatterer map pixels per mm^2 . Assuming that roughly $1/10^{\text{th}}$ of all pixels are populated with non-zero scatterers based on our sparsity constraint, the above results in a scatterer density of 250 per mm^2 . This well exceeds the threshold of 100mm^{-2} given by Oosterveld et al. [28] for a fully-developed Rayleigh distribution of speckle intensities, and hence satisfies (c).

Mapping from scatterer space to RF space. Convolution of a scatterer map with the PSF sampled at the same resolution creates an RF image that is the size of the scatterer map, with the RF line number based on our convention above being a multiple k of the original RF image. To downsample to the size of the input RF image (i.e., for simulating an image), every k^{th} RF line of this convolved image is picked. This can be done by applying a decimation operator S accordingly, on the vector of image pixels. A pixel of the downsampled RF image is a linear superposition of contributing scatterers within a PSF kernel radius. Conceptually, the same operator can be used to construct the convolution matrix as $A=SH$, $S \in \mathbb{R}^{m \times n}$, $H \in \mathbb{R}^{n \times n}$, where H is an $n \times n$ convolution matrix in scatterer space, and S is the decimation operator picking every k^{th} row to obtain an $m \times n$ matrix. In practice for simulation, we numerically compute only the required decimated rows in A .

C. Domain decomposition

Attempting to solve for an entire US image with high axial resolution and possibly multiple measurements within a single linear system can quickly exceed the memory and computing capacities of most computers. To make the problem more tractable, we propose a strategy that can handle arbitrarily large images with arbitrarily high resolutions. As illustrated in Fig. 6(c), we partition the images into smaller domains that can be easily solved individually, starting from top-left in a greedy fashion. The individual solutions are combined into a single scatterer map. Incorporating already-solved scatterers into new blocks as boundary constraints avoids artifacts at block-seams. In particular, we subtract the speckle contribution of the previously computed scatterers (in the blue upper-left borders) from the RF measurements b_i of the current block, and accordingly constrain the scatterers x_i in the current block to 0 in that border region (since they are computed/accounted for in the earlier blocks). This effectively constrains these scatterers in the blue border region to their previously computed values. For this purpose, we generalize the objective in Eq. 2 to contain a regularization term with element-wise weighting, i.e. $\lambda \|Wx\|_1$. The diagonal elements W are set such that $W_{ij}=1$ in the interior of a block and $W_{ij}=10^6$ in the blue border regions, resulting in a large penalty for non-zero scatterers. We use a margin/overlap of width b_l and b_a of at least half the size of the PSF kernel to avoid seams in the simulation along the block borders, to ensure that all RF signal observations inside the current block can be explained by scatterers including the block margin. This heuristic guarantees that the solver finds a feasible solution taking the surrounding scatterer contributions into account. Although this solution may not be the global optimum, we found that it is sufficient for the level of accuracy that we demand from our optimization.

Beam-steered images. In the case of multiple steered images in our block-wise solution, all domains corresponding to the same index in Fig. 6(d) are solved simultaneously in a single iteration. To find these domains, we define the patch to solve in the scatterer solution space, and project it to each steered images and use those regions in Eq. (5).

D. Implementation

We use the Alternating Direction Method of Multipliers (*ADMM*) [5] for solving the objective in Eq. (2). *ADMM* is known to be efficient for large problems where moderate precision is acceptable, unlike accurate but less scalable Interior Point methods [20]. In particular, we use the *ADMM* solver YALL1 [43], which supports *RLAD* objectives with positivity constraints. A detailed description of how such problems can be converted into an ADMM formulation is given by Boyd et al. [5]. In our implementation, convolution matrices were explicitly defined in Matlab using a sparse representation, with a typical sparsity of 99.96% for, e.g., the experiment in Fig. 7. All results were generated using MATLAB on a Intel Core i7-4900MQ CPU with 2.8 GHZ and 24 GByte memory. **Post processing.** The final B-mode image is obtained from the scatterer map after convolution, envelope detection, time-gain compensation, and dynamic-range (log) compression, using the post-processing pipeline provided by the Amplio Toolkit from Ultrasonix (Richmond, BC, Canada) (see Fig. 4, right).

IV. RESULTS

In the following we denote our scatterer reconstruction method as *ScatRecN*, where N is the number of input images used for reconstruction. The input images are taken in regular angular steps over an angular range of $\pm M^\circ$, where M typically ranges from 5° to 30° . For instance, *ScatRec5 $\pm 20^\circ$* denotes our multi-view reconstruction method using image observations at angles $\{-20, -10, 0, 10, 20\}^\circ$. Since the goal of our method is ultrasound simulation, we compare convolution-based [4] simulated images using scatterer maps from our method with ground-truth (GT) images from a known scatterer continuum. *ScatRec1* not only constitutes the simplest instance of our algorithm, but it is also used as a baseline in this paper. Note, however, that *ScatRec1* already profits from our contributions of using the constrained *RLAD* formulation in Eq. (2) and the domain decomposition of input image (Sec. III-C) for robustly handling sparse large systems. The above are indeed advantages of *ScatRec1* over the scatterer reconstruction method in [20], which is only suited for small patches and unable to solve large systems, e.g., entire ultrasound image frames.

Experimental setup. *ScatRecN $\pm M^\circ$* is used to reconstruct a scatterer map from RF images. This map is subsequently used to generate simulated images at several angles (see Fig. 7(a)), which are compared to expected or known (ground truth) images at such angles. For evaluation, we present qualitative and quantitative results from a computer-generated phantom, a gelatin phantom, and clinical ultrasound images.

Image error metrics. For quantitative evaluation of the simulation results in Tab I, II, III, three global features, denoted as

I , SNR , CNR , and one local and one histogram feature, denoted as MAE and χ^2 -histogram distances, are used to compare the simulated and ground truth B-mode (envelope) images.

The mean image intensity I is computed as $I = \frac{1}{n} \sum_{j=1..n} s_j$ from envelope image intensities s_j . Signal-to-noise ratio is computed as $SNR = \frac{\mu}{\sigma}$. This, according to theory [28], should be close to 1.91 for Rayleigh-distributed ultrasound speckles. Contrast-to-noise ratio is computed as $CNR = |\mu_{s_1} - \mu_{s_2}| / (\sigma_{s_1} + \sigma_{s_2})$, where s_1 and s_2 denote intensity values of two contrasting ultrasound tissues, e.g., intensity values in the inclusion and the surrounding tissue in Fig. 7, respectively. We present the normalized error in global metrics SNR and CNR as a percentage, computed as $100|F_s/F_t - 1|$, where F_t (F_s) is the ground truth (simulated) metric value. For instance, for an average intensity $I_t = 80$ in the ground truth image, and $I_s = 60$ in the simulated image (which accordingly looks darker), this normalized metric would yield $100|60/80 - 1| = 25\%$ error. A perfect fit then has 0% error, while under- and over-estimation both yield positive values.

As a local metric, the mean absolute error $MAE = \frac{1}{n} \sum_{j=1..n} |s_j - t_j|$ is used, where s_j (t_j) are the intensity values of the simulated (ground truth) image. To isolate local differences from global intensity difference (which can arguably be compensated by a global brightness equalization), prior to MAE the compared images are brightness-normalized by shifting their mean intensity I to 100. A value near 50% points to a marginal local correlation between the two images.

The last metric is the commonly used χ^2 distance between the intensity histograms of ground truth and simulated images.

Another popular texture metric SSIM [41] was considered but not used in this work, since we found in a recent study [24] that SSIM performs poorly for quantifying perceived similarity between ultrasound image patches for evaluating simulations. **Field II simulations.** Fig. 7(b) illustrates the results of our method for rotated views of a 8×8 mm box-shaped numerical phantom with a spherical inclusion, placed 10 mm away from the transducer. Field II was used for simulation using 9K scatterers and a speed of sound of 1540 m/s. We simulated a 6.0 MHz linear transducer with a sampling frequency of 40.0 MHz, a dynamic receive focus and a single transmit focus at 10 mm, which allows us to study both in- (top) and out-of-focus (bottom) image regions. The transducer width was set to 30 mm assuming 192 RF lines, in order for all steered images to capture the complete phantom. The resulting images were then cropped to the region of interest containing the phantom.

The top and the middle rows show the simulation results for the scatterer maps generated with $ScatRec1$ and $ScatRec7 \pm 30^\circ$, respectively, from three viewing angles. The last row of images show Field II-simulated observations for the same three viewing angles, which constitute the ground truth. For $ScatRec1$, the speckle appearance changes significantly, proportionally to the rotation angle. In particular, note that for a 30° rotation the contrast of the inclusion to surrounding tissue becomes very low – almost indistinguishable. For $ScatRec7$, the speckle appearance stays visually closer to the ground truth in terms of speckle appearance. While the individual speckles may differ for a 30° rotation (difference

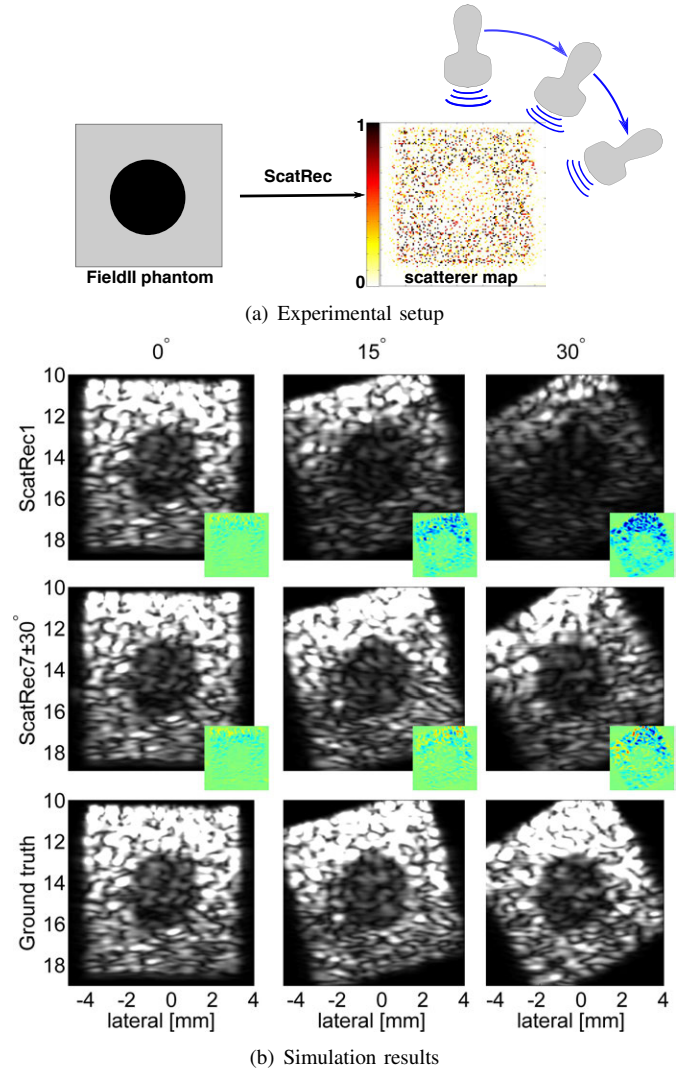


Fig. 7. (a) Setup of a Field II experiment for transducer rotations around a simulated phantom. (b) Our method compared to the ground truth for sample rotated views from the Field II experiment (differences shown in close-ups).

images shown in the insets), properties of the ground truth images are preserved. The benefits of using 7 images for reconstruction instead of a single image is also highlighted by the difference images shown in the insets.

Tab. I compares a selection of metrics from the above-mentioned simulations shown in Fig. 7, using the same rotation angles $0^\circ/15^\circ/30^\circ$. For SNR we evaluated the tissue surrounding the inclusion. The metrics for $ScatRec7 \pm 30^\circ$ are seen to be closer to the ground truth than $ScatRec1$ for the

TABLE I
ERROR METRIC COMPARISON FOR ROTATED IMAGES SHOWN IN FIG. 7 WITH 1 OR 7 INPUT IMAGES. FOR $SCATREC1$, THE ERROR INCREASES QUICKLY FOR ROTATED VIEWS BECAUSE THE SOLUTION IS ONLY VALID FOR THE INPUT VIEW. $SCATREC7$ AVOIDS THIS PROBLEM BY OPTIMIZING OVER RANGE OF INPUT ANGLES.

Metric	I (%)			SNR (%)			CNR (%)			MAE (%)			$\chi^2 [\times 10^{-3}]$		
	0°	15°	30°	0°	15°	30°	0°	15°	30°	0°	15°	30°	0°	15°	30°
1±00	1.4	36.7	65.6	0.2	10.4	15.2	1.0	7.0	40.8	4.5	29.8	41.4	0.2	1.6	8.0
7±30	1.6	1.6	0.9	1.3	1.3	2.8	1.6	1.3	2.2	7.3	17.4	29.1	0.9	0.2	0.5

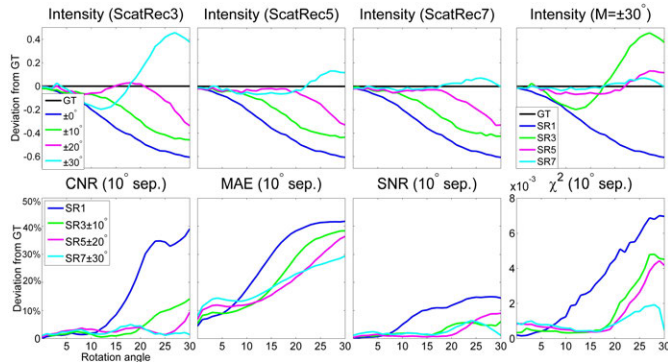


Fig. 8. Deviations from ground truth (GT) for $ScatRecN\pm M^\circ$ (SR) simulations of a Field II-simulated phantom with respect to rotation angle (i.e., values deviating from 0 indicate worse fit). Top row: fluctuations from mean intensity with respect to GT for $ScatRecN\pm M^\circ$ in $[-1..1]$, varying M for fixed N and vice versa. Bottom row: Deviations from GT for other used metrics, using $ScatRec3/5/7$ with 10° separation between steering angles.

rotated views at 15° and 30° . For the original 0° angle, since $ScatRec1$ overfits its reconstruction to that one angle, it gives lower errors, which however quickly degrades and cannot generalize to the multi-view problem. $ScatRec7\pm 30^\circ$ still performs comparably and well at 0° angle. This indicates that the multi-view optimization is not negatively influenced by the additional information and the potential noise in steered images, while improving the reconstructions even at unseen (un-trained) angles, such as 15° missing in $ScatRec7\pm 30^\circ$ input. CNR is highly relevant in a training simulator, since a different CNR (potentially the difference between a pathology being detected or missed) could compromise simulator fidelity or worse lead to a false training of the user.

In Fig. 8 we investigate the reconstruction errors of the Field II phantom for rotations with 1° increments. In Fig. 8(top) the deviation of mean intensity I from the ground truth is shown for different versions of $ScatRecN\pm M^\circ$. To collocate all metrics in one plot, we normalized them all to a scale $[-1, \dots, +1]$, i.e. displaying $I_s/I_t - 1$. As expected, near 0° the mean intensity is close to the ground truth for all combinations of N and $\pm M^\circ$, but typically increases proportionally to the rotation angle. In general, having optimized for an angular span $\pm M^\circ$, the mean intensity error degrades relatively slowly until that rotation angle, and more substantially for over M° (due to the lack of observations outside that range). For large $\pm M^\circ$, increasing the number of intermediate views with higher signal-to-noise ratio reduces deviations from the ground truth as well as brightness fluctuations around the baseline between rotation angle 0° and 30° . This is summarized in the top right plot of Fig. 8. In the bottom row of Fig. 8, we show various error metrics based on increasing N for a fixed 10° increment between the N consecutive steering angles. For these experiments we see a behavior similar to that before; i.e., small N and $\pm M^\circ$ can achieve an excellent fit for small rotation angles. For rotation angles $> M^\circ$, however, the reconstruction error increases significantly and needs to be fixed by adding more observations. $ScatRec7\pm 30^\circ$ has a low reconstruction error over all rotation angles, and exhibits minor fluctuations in reconstruction quality for the chosen metrics.

In Tab. II, some illustrative metrics are tabulated for a detailed quantitative evaluation of the Field II phantom in Fig. 7, using a dense set of rotation simulations and reconstructions. We evaluate reconstructions for simulations with sample rotations at every 1° from 0° to 30° . The results presented in the table are average metrics over all 31 rotation angles. We use a selection of 3 metrics (I , MAE , CNR) to assess quality dependence of $ScatRecN\pm M$ on the number of input images N and the angular span M , as well as on the step size between consecutive steering angles. Clearly, $ScatRec$ instances using multiple images perform better than $ScatRec1$ in almost all cases. An important conclusion from Tab. II is that increasing the angular range M in general produces a better fit over the whole range of rotations, up to a limit of angular separation between input images. This can be seen best in the 4th column of each metric (*best N*), which shows the best result among $ScatRec3/5/7$ for a particular M . For too large angular separation between input images, most notably for $ScatRec3\pm 30^\circ$, the similarity with the ground truth decreases quickly. This fact can be explained by the decreased signal-to-noise ratio for large steering angles, which are 2 of the 3 input images herein. By increasing the number N of input images from 3 to 5 or 7, better results can be achieved even for a large $\pm M^\circ$. This behaviour can be most clearly observed for mean intensity I .

In summary of Field II phantom results, increasing the number of the input images N and the range $\pm M^\circ$ both achieves smaller error to the ground truth; This is further highlighted by showing the overall smallest (largest) deviation in row/column *best N/M* of Tab. II in blue (red). From the given set of configurations, we would hence recommend to use $ScatRec7\pm 25^\circ$ or $\pm 30^\circ$ for best quality, where error metrics are the lowest. Theoretically, the optimal separation between individual steering angles is connected to the maximum decorrelation between steered PSFs, depending on center frequency and many other variables that are not easily quantifiable. The results indicate that an optimal separation empirically lies between 7–10°. As a tradeoff, however, increasing N requires longer computation times, with average running times for scatterer reconstruction of 23/70/117/165 min for $ScatRec1/3/5/7$, respectively.

To test the dependence of simulation results on the accuracy of PSF estimation, we shifted the focus depth in the Field II used as input to our method from 10 mm to 10.7 mm (by

TABLE II

SPECKLE FEATURE COMPARISON FOR CONTINUOUS ROTATION FROM $0^\circ..30^\circ$ USING THE SETUP SHOWN IN FIG. 7. IT IS SEEN THAT, FOR ACHIEVING A LOW AVERAGE ERROR, IT IS IMPORTANT TO INCREASE BOTH THE NUMBER OF INPUT OBSERVATIONS N AND THE ANGULAR RANGE M .

Metric	I (%)				MAE (%)				CNR (%)			
	3	5	7	best N	3	5	7	best N	3	5	7	best N
$\pm 05^\circ$	27.3	27.7	27.3	27.3	22.4	22.8	23.1	22.4	12.8	18.5	30.9	12.8
$\pm 10^\circ$	21.7	21.7	21.8	21.7	21.0	20.6	20.7	20.6	5.4	6.8	10.9	5.4
$\pm 15^\circ$	15.9	16.3	16.9	15.9	20.1	19.8	19.6	19.6	5.9	3.3	5.1	3.3
$\pm 20^\circ$	8.0	9.4	10.6	8.0	19.8	18.8	19.3	18.8	3.9	3.0	3.5	3.0
$\pm 25^\circ$	8.5	4.6	4.1	4.1	20.3	19.6	18.3	18.3	3.5	2.6	2.2	2.2
$\pm 30^\circ$	18.3	5.6	2.3	2.3	27.5	19.5	18.6	18.6	8.6	2.0	2.2	2.0
best M	8.0	4.6	2.3		19.8	18.8	18.3		3.5	2.0	2.2	
ScatRec1				34.2				26.2				15.1

approximately a PSF kernel footprint) in the axial direction. This slightly diminished the similarity to the ground truth, e.g., the best match error for I in Tab. II increases from 2.0% to 4.4%, and the best match error for MAE increases slightly from 18.3% to 20.9%. This demonstrates some relative robustness, but also indicates the need and importance of estimating a good PSF that is required as an input to our method.

Gelatin phantom. We next demonstrate results using phantoms from actual ultrasound scans. We used a SonixTouch (Ultrasonix, Richmond, BC) machine with L12-5 linear transducer, placed over a gelatin phantom with cellulose as scattering media. In these experiments, the PSF was estimated from the input images [21]. The images were collected using a multi-static imaging sequence with full-aperture reception using SonixDAQ. From this rich data collection, any electronically steered focused-transmit could then be reproduced in a post-processing step using synthetic aperture beamforming. *ScatRec3* in Fig. 9(a) uses 3 observations of the gelatin phantom and the estimated steered PSFs (mid-row) to simulate the input observations from the reconstructed scatterer map. The results in the bottom row of Fig. 9(a) are in excellent visual agreement with the log-compressed B-mode input images. Fig. 9(b) shows simulations of rotated views of the phantom, to demonstrate the superiority of *ScatRec3*±10° with respect to *ScatRec1* for envelope images. Similarly to the Field II experiments, it is seen that *ScatRec1* can reproduce the tissue with excellent agreement, but only when considering the exact same view-point. When images from different view-points are required, *ScatRec3*±10° is superior, even after exceeding 10° of rotation. The main visual difference to the input is the subdued specular reflection from the (isoechoic) spherical inclusion. Said reflection violates the assumption of purely diffuse scattering and thus cannot be represented in the scatterer space consistently over a range of viewing angles.

Rayleigh statistics is a common measure to quantify ultrasound speckle, which we aim to model and simulate; hence is presented next as a comparative evaluation. Fig. 9(c) depicts the histogram of the 0° (envelope) input image and compares it to the histograms of the envelope images from *ScatRec1* and *ScatRec3*±10°, after rotating the reconstructed scatterer maps by 30°. The histogram for *ScatRec3*±10° is in better agreement with the histogram of the original image compared to *ScatRec1*, and close to an ideal Rayleigh distribution. The patches of the envelope images used for measuring the speckle statistics are shown below the histograms.

In vivo experiment. In Fig. 10, we show our results from the ultrasound examination of the breast, with the hypoechoic inclusion indicating a cyst. The images were collected using the same Ultrasonix system above for the phantom experiments, with data acquired with a multi-static sequence. Steered images with 5° increments within a ±30° range were then generated using synthetic aperture beamforming. We computed scatterer maps using *ScatRec1* and *ScatRec7*±30°, using only the steered images at 0°, ±10°, ±20°, and ±30° m as input. We then simulated steered images at all 13 angles {-30, -25, ..., +30} using convolution-based simulation from scatterers reconstructed with *ScatRec1* and *ScatRec7*. This experiment hence constitutes a test of how well our algorithm optimizes

images both at the given input angles and also at in-between angles that were not used in optimization, namely ±5°, ±15°, ±25°. Some acquired and simulated images as well as their differences are shown in the figure. It shows that *ScatRec7* resembles the ground truth for all steering angles, whereas *ScatRec1* produces images different from the ground truth at increasing angles. Images with *ScatRec1* appear rather like a simple cropping from the 0° image, since the additional angles are not taken into account.

In Tab. III, these results are corroborated by a quantitative evaluation on the enveloped images. The angles that were used as input for *ScatRec7*±30° are shown in bold. *ScatRec7* performs substantially better than *ScatRec1* for angles ≥15°, and stays relatively close to the ground truth for both the input angles and in-between angles. As expected, the most significant deviations from the ground truth for *ScatRec7* are reported based on local per-pixel comparison MAE . This is nevertheless not an issue for the purpose of training simulation, which is not about individual speckles but about perceived tissue appearance.

Use scenarios: Imaging parameters and Scene editing. Fig. 11 demonstrates the performance of our algorithm for a single observation of a liver *in vivo* using a convex abdominal probe. In Fig. 11(a) B-mode visualization of the input image (a) and the acquired scatterer map (b) are shown, downsampled to 0.5% of the original scatterers for the purpose of visualization. Deconvolution was performed in the polar coordinate frame of the original RF lines before scan converting into the Cartesian domain; demonstrating the use of the introduced techniques for convex transducers. In Figure 11(c), a B-mode image is simulated from the scatterer map at the same 4.5MHz as the input image, showing a simulated image visually very similar to the original one. The difference map goes to ±10% of the maximum image brightness, with a negligible average. Alternatively, we use 2.0MHz center-frequency for simulation, which produces a different speckle appearance, with small features – less resolved as expected (Figure 11(d)). One can also easily change the transmit focus depth or other beamforming parameters in simulation time.

Another novel use of scene editing in the scatterer domain is shown in Fig. 12. In Fig. 12(a) we show content “copy-paste” in the scatterer domain, where a vessel is “transplanted” to another location. Note in the blown-out image (c) that the transferred patch smoothly blends into the surrounding tissue,

TABLE III

ERROR METRIC COMPARISON FOR ROTATED IMAGES SHOWN IN FIG. 10 WITH 1 OR 7 INPUT IMAGES. FOR *SCATREC1*, IN VIVO RESULTS AGAIN DEMONSTRATE THE REDUCED QUALITY OF ROTATED ANGLES. *SCATREC7* AVOIDS THIS PROBLEM BY OPTIMIZING OVER RANGE OF INPUT ANGLES.

Method	Metric	0°	5°	10°	15°	20°	25°	30°
<i>ScatRec1</i> ±00°	I (%)	6.4	0.1	21.9	30.6	44.1	47.8	57.8
<i>ScatRec7</i> ±30°	I (%)	3.7	5.8	12.3	6.5	5.2	6.3	10.9
<i>ScatRec1</i> ±00°	SNR (%)	3.2	1.9	21.1	25.8	37.3	38.0	51.5
<i>ScatRec7</i> ±30°	SNR (%)	4.6	2.4	18.3	14.4	9.9	4.5	14.5
<i>ScatRec1</i> ±00°	MAE (%)	7.0	19.0	26.5	36.2	49.0	57.8	64.5
<i>ScatRec7</i> ±30°	MAE (%)	6.4	17.5	16.6	18.3	18.2	25.3	34.8
<i>ScatRec1</i> ±00°	χ^2 [$\times 10^{-3}$]	2.5	4.6	9.6	33.6	38.1	28.4	29.0
<i>ScatRec7</i> ±30°	χ^2 [$\times 10^{-3}$]	4.5	12.7	19.1	6.4	14.6	3.8	12.2

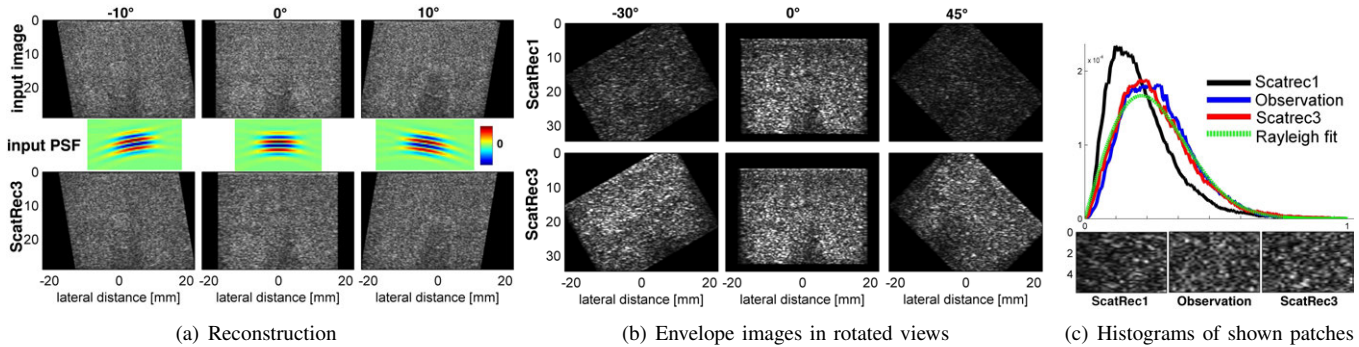


Fig. 9. (a) Reconstruction of input images for gelatin phantom, using PSF estimated from said images, (b) *ScatRec1* vs. *ScatRec3*±10°, (c) Rayleigh statistics.

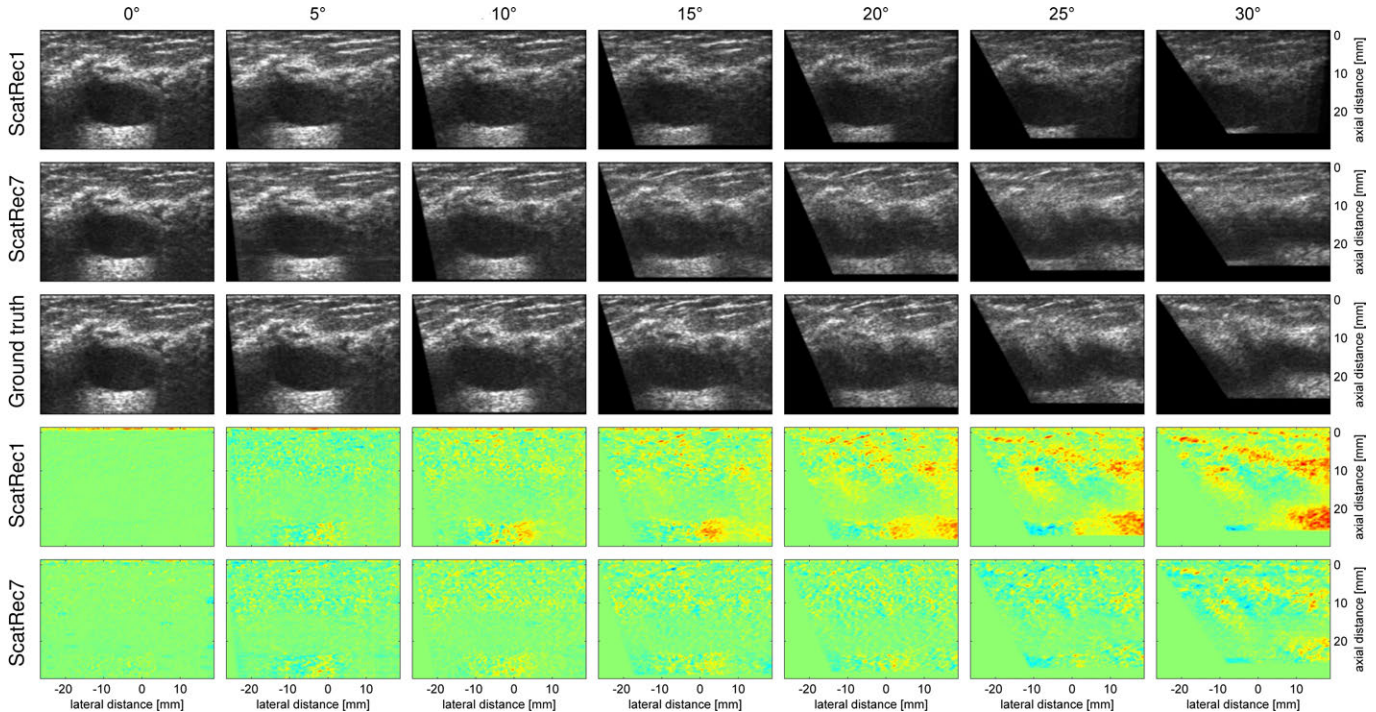


Fig. 10. Comparison of simulation results using *ScatRec1* or *ScatRec7*±30°, respectively, to *in vivo* scans of cyst in female breast (Ground truth), which were obtained using beam steering. Only steered images for 0°, 10°, 30° were used as input for *ScatRec7*±30°, whereas images for in-between angles of 5°, 15°, 25° are generated as novel views. The difference colormaps range from green (0) to red (±100%), highlighting the better accuracy of *ScatRec7*±30°.

while the editing in the B-mode domain is observed to create disturbing seams/artifacts. In Fig. 12(b), the distortion caused on the skin by the pressure from a *convex* probe is undone in the scatterer domain in order to simulate *linear* transducer imaging at yet another imaging frequency of 6.6MHz. Compared to B-mode editing, the speckle pattern would be affected minimally by distortion using our method, because the editing is performed *prior to* convolution.

Scene statistics. Tab. IV tabulates the important settings in different experiments: transducer center frequency (*CF*), sampling frequency (*SF*), transducer type (*Type*), transducer field-of-view (*FOV*), RF image resolution (R_{rf}), scatterer map resolution (R_{sc}), proportion (k) between lateral speckle vs. scatterer resolution, number of input observations ($\#N$), and used *domain decomposition grid* (DDG). Lateral scatterer resolution is a multiple k of RF line number, where k is computed as $\lfloor \Delta_l / \Delta_a \rfloor$, as described in Sec. III-B. For datasets

Phantom and Breast, the size of a scatterer image is enlarged laterally by adding left and right borders of 7 mm each, to be able to contain all the steered images within a scatterer map as discussed in Sec. III-A. Besides the three varying parameters listed in Tab. IV, i.e. k , $\#N$, and DDG, 4 other constant parameters were used for all scenarios: regularization factor $\lambda=0.005$, confidence parameter $\beta_{max}=60^\circ$, and the decomposition border margins $b_l=160$ pixels and $b_a=70$ pixels.

We experimented with varying the value of k . For example, we used a value of $k=3$ for *ScatRec3*± M° , which is the critical point where $Ax=b$ is no longer underconstrained. For the Field II phantom in Tab. II and *ScatRec3*± M° , CNR error to the ground truth increased to 26.5% (±5°), 16.7% (±10°), 9.7% (±15°), 4.2% (±20°), 6.2% (±25°), 10.1% (±30°), which constitutes an increase by 13.7%, 11.3%, 3.8%, 0.4%, 2.8%, 1.5% w.r.t. the setting $k=8$.

Parameters. In the remaining result section we investigate

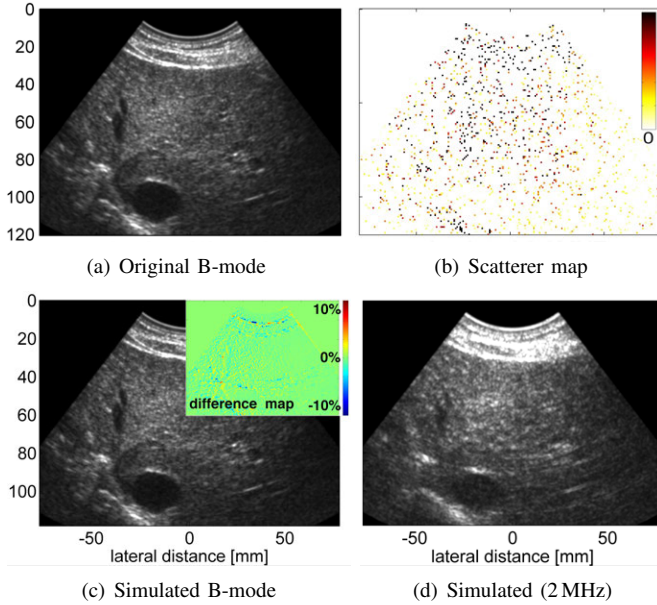


Fig. 11. Using an *in vivo* observation of a liver, the scatterer map (b) is computed from the input image (a), and can be forward-simulated using the original transducer frequency (c) or a different frequency (d), hence allowing rapid creation of novel images with varying parameters.

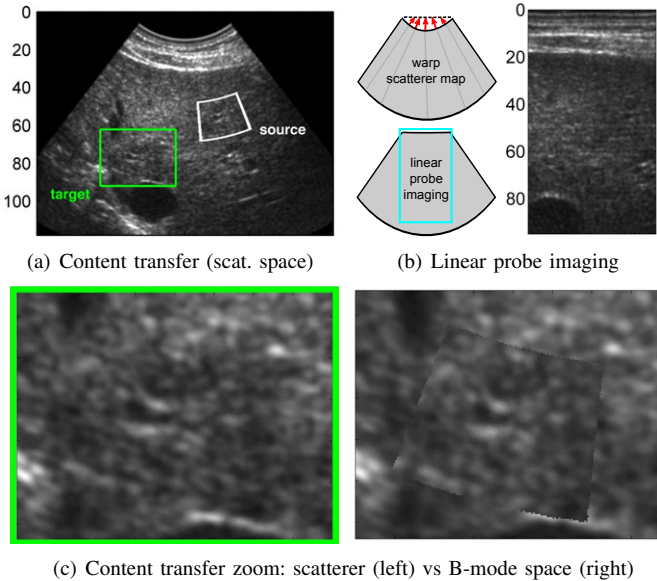


Fig. 12. Scene manipulation in scatterer space. (a) Cropping and pasting content seamlessly to another place, shown in close-up (c), left. Note the seams in B-mode content transfer (c), right. We can undo the distortion of the original scatterer map to simulate a typical linear probe image (b).

the influence of some parameters and optimization choices, in particular the norms for the chosen objective, λ_{opt} , and the confidence weights c_i , on the performance of $ScatRecN \pm M$, by using the phantom in Fig. 7. Example plots from these experiments are given in Fig. 13.

Using $ScatRec3 \pm 10^\circ$ as example, we first analyze the influence of varying the regularization constant λ_{opt} , from values 0.01, 0.005 (used for the paper), to 0.001 (=less regularization). Using contrast-to-noise ratio (CNR) error as an example, it can be shown that for higher regularization

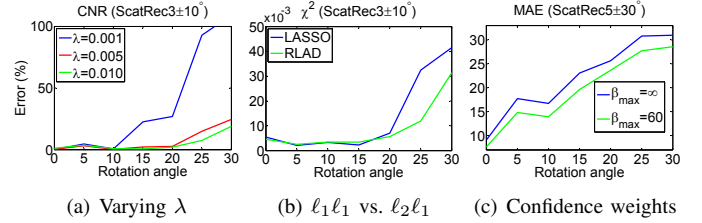


Fig. 13. (a) A sufficiently large regularization constant λ is important for many-angle reconstruction. (b) In our tests, *RLAD* has been shown to produce marginally lower error values than *LASSO* with its mixed $\ell_2\ell_1$ norms. (c) Allowing linear falloff of confidence with respect to steering angles reduces image errors.

values $\lambda_{opt}=0.01$ and $\lambda_{opt}=0.005$, CNR stays relatively low with an average over 7 rotation angles of 4.96/5.59%. For $\lambda_{opt}=0.001$, the CNR error increases significantly (36.70%). More specifically, as shown in Fig. 13(a) the error stays low for angles $\leq M$ (0%, 4.58%, 0.60%) and increases rapidly for angles $>M$, showing that this constitutes insufficient regularization. A known problem of regularization methods is that the solution to the original problem is underestimated, leading to an average error in intensity values I of 14.05/21.87/23.49 for $\lambda_{opt}=0.01/0.005/0.001$. Thus, we chose $\lambda_{opt}=0.005$ because it is a good compromise with just enough regularization.

Using $ScatRec3 \pm 10^\circ$, we compare the performance of the used *RLAD* (i.e., an $\ell_1\ell_1$ objective) with the more common *LASSO* (i.e., an $\ell_2\ell_1$ objective). When averaging over 7 simulated angles as in the previous experiment, we obtained errors for *RLAD* / *LASSO* with the default $\lambda=0.005$, as $I=21.87/22.62\%$, $SNR=3.95/4.38\%$, $MAE=20.88/21.19\%$, $\chi^2=0.018/0.022$, $CNR=5.58/6.85\%$, indicating a slightly but consistently lower error of *RLAD* compared to *LASSO*. Fig. 13(b) shows that *LASSO* performs significantly worse for transducer rotation angles $\geq 20^\circ$. We reached the same conclusions after repeating this experiment for another regularization parameter $\lambda=0.01$, in which case again *RLAD* performed consistently better than *LASSO* for all metrics.

As shown in Fig. 13(c), we investigated the influence of using confidence weights c_i , with respect to the steering angles β_i on the accuracy of our results, using $ScatRec5 \pm 30^\circ$ on the phantom in Fig. 7, comparing $\beta_{max}=\infty$ and $\beta_{max}=60^\circ$. As a representative example, we measure the metric errors averaged over 7 simulated rotation angles with 5° separation from 0° to 30° , for $\beta_{max}=60^\circ/ \beta_{max}=\infty$, leading to $I=5.49/9.02\%$, $SNR=4.18/5.54\%$, $MAE=19.43/22.00\%$, $\chi^2=0.009/0.014$, $CNR=2.14/3.37\%$, indicating the advantage of the β_{max} parameter used. Similarly, individual metric values for each rotation angle were seen to be consistently better when using varying confidence weights c_i (depicted in Fig. 13(c)) for a

TABLE IV
SCENE STATISTICS

Input	CF/SF	Type	FOV	R_{rf}	R_{sc}	k	#N	DDG
Field II	6.0/40MHz	Lin.	9mm	64×448	504×448	8	7	2×4
Phantom	6.6/40MHz	Lin.	38mm	128×1800	2520×1800	14	3	5×9
Breast	6.6/40MHz	Lin.	38mm	128×2000	2520×2000	14	7	5×9
Liver	4.5/20MHz	Conv.	75°	192×3136	1920×3136	10	1	4×16

sample metric). Overall, varying weights constitute a clear improvement as compared to constant c_i with $\beta_{max}=\infty$. Hence we conclude that reducing the influence of extreme steering angles to account for a deteriorating SNR and errors in assumptions (e.g., PSF rotation) is justified.

We next investigate the memory consumption of our sparse matrices with respect to N and the used domain decomposition. For *ScatRec1* partitioned into 4×2 domains (4 axial, 2 lateral partitions), a single convolution matrix A is a 10296×82368 sparse matrix with a memory footprint of 550 MB. As expected, for *ScatRecN*, the size of the matrix and the memory consumption increases roughly by a factor of N (e.g., 1550 MB for *ScatRec3*). Using *ScatRec3* with 4×1 domains, the memory footprint already grows to 2845 MB. Note that for the full 3D scatterer reconstruction problem, it is expected that the sparsity of both A and resulting scatterers x increases by a significant amount compared to the 2D problem.

Since optimization algorithms are typically of polynomial complexity, a partitioning into smaller solutions can theoretically speed up computations. We evaluated the times needed to compute a scatterer solution with respect to two different domain decompositions for varying N . For $4\times 2/4\times 1$ partitions, we obtain for $N=1$: 53/45 min, $N=3$: 125/138 min, $N=5$: 158/151 min. Hence we conclude that the render times are roughly comparable, and that in our experiments the overhead of more overlaps on the borders and the repeated allocations of sparse matrices roughly balance out a theoretical advantage of many smaller solutions regarding algorithmic complexity.

V. DISCUSSION AND LIMITATIONS

In this work, we reconstruct the scatterer map of *entire* US images in RF space, and use the reconstructed maps directly for simulation. RF space allows us to retain phase information about constructive and destructive interference effects between nearby scatterers, as opposed to solving the problem in the demodulated signal space [20], i.e. after envelope detection. Also, this method faithfully captures small non-statistical variations in the scatterer map, which are prevalent in real tissue and important for the realism of the simulation. From the reconstructed maps, a homogeneous US image patch can be used to estimate a parametrized scatterer model of the underlying tissue [20]. The resulting parametrization can then be used to instantiate scatterer maps for new structures of the same tissue, inpaint larger models, and generate arbitrary geometrical scenes from a tissue library.

We investigated *ScatRec* for up to 7 images in the evaluation, since our experiments suggest that beyond 7 images, the gain in quality is minor as compared to the increase in computation time. 7 images are still small enough for efficient inverse-problem computation, and the rapid acquisition of 7 electronically beam-steered images is conceivable well under a second where large motion is minimal. Any such motion indeed exists in the two *in vivo* datasets, where the results are still consistent with simulations and expectations. Note that we aim for offline processing, whereas the resulting scatterer maps can be later used in real-time simulations. We envision scatterer reconstruction to be performed only once for

a dataset, and the resulting scatterers to be fed into an online simulator, e.g. [23], using the forward pipeline.

As an example of computation time, the scatterer reconstruction for the dataset Breast in Fig. 10 took 193 min for *ScatRec1* and approximately 1315 min (≈ 22 h) for *ScatRec7*, respectively. The computation time for multiple views is justified by robustness of the speckle appearance with respect to varying view parameters, which we show in many examples. In this work, image simulation (forward-problem) computations were in the range of seconds to minutes, using an unoptimized Matlab implementation; e.g., 51 s for Fig. 7. Nevertheless, it is possible to conduct simulations in milliseconds by using scatterers extracted herein as input to dedicated GPU-based simulations, e.g. [6], [23], for generating images interactively.

Reflections from large-scale structures and other directional artifacts appearing in the input images, including ultrasound shadowing effects due to absorption and reflections, are currently not handled separately in our implementation and hence may be treated incorrectly as a property of the tissue itself. We believe that using ℓ_1 regularization already helps to suppress some of these directional artifacts, since strong reflections appearing in only a subset of the input images are treated as outliers. Ideally, however, we would identify the diffusely scattering parts (e.g., using Rayleigh fitting) and use *only* those for scatterer reconstruction, while modeling directional ultrasound interactions via other methods, such as GPU-based raytracing techniques [6], [23].

Attenuation is modeled and compensated by a time-gain compensation step, prior to using the ultrasound RF signal in the *ScatRec* inverse-problem. We herein did not take local attenuation changes into account, but it is conceivable to use more refined models in the future to estimate local attenuation, similarly to [16]. Sound-speed is currently assumed to be constant in our implementation, ignoring aberrations as well different wave-paths in the tissue [33]. Sound-speed changes can also potentially be acquired [31] and simulated as a parameter in raytracing techniques [23].

A logical step forward is to extend our method to acquire 3D scatterer volumes. This may require a novel approach for reducing algorithmic complexity and the memory footprint. It is, for example, conceivable to exploit the fact that our deconvolution matrix is approximately block-circulant, as for block-circulant matrices it is possible to efficiently use fast Fourier transform for solving the inverse problem [12]. To account for the varying PSF, a similar partitioning of the domain into sections of locally constant PSFs could be used.

In related work, we investigated alternative uses of ultrasound simulation of novel content other than training simulation. As recent examples, simulated images have been used for the validation of ultrasound image-analysis methods [29], [34], [35]. The proposed method can be used to produce such realistic content. Due to interactive frame rates of modern simulation methods it is also conceivable to use them in example-based learning, by rapidly generating ultrasound images from varying input parameters. Furthermore, scatterer maps may have potential diagnostic value for the detection of pathologies, due to changes in tissue composition during pathological processes.

VI. CONCLUSIONS

We have presented a novel technique to reconstruct a scatterer representation of the tissue. In ultrasound simulations, these scatterer maps can be used to create realistic images of tissue under varying viewing angles and transducer profiles. Scatterers also represent the tissue in a different space, where scene editing operations such as copying, adding, distorting the anatomy can be performed easily without image artifacts. With electronic beam steering, we acquire a sufficient number of input images for a solution robust in simulations; without any need for a mechanical setup or measuring frame. Results from numerical and physical phantoms as well as *in vivo* images have been presented, for both convex and linear probes. We have presented both qualitative and quantitative results, demonstrating the value of our method.

REFERENCES

- [1] Aiger, D., Cohen-Or, D.: Real-time ultrasound imaging simulation. *Real-Time Imaging* 4(4), 263–274 (1998)
- [2] Alessandrini, M., Craene, M.D., Bernard, O., Giffard-Roisin, S., Allain, P., Waechter-Stehle, I., Weese, J., Saloux, E., Delingette, H., Sermesant, M., D’hooge, J.: A pipeline for the generation of realistic 3d synthetic echocardiographic sequences: Methodology and open-access database. *IEEE TMI* 34(7), 1436–1451 (2015)
- [3] Alessandrini, M., Maggio, S., Poree, J., Marchi, L.D., Speciale, N., Franceschini, E., Bernard, O., Basset, O.: A restoration framework for ultrasonic tissue characterization. *IEEE TUFFC* 58(11), 2344–2360 (2011)
- [4] Bamber, J.C., Dickinson, R.J.: Ultrasonic b-scanning: a computer simulation. *Physics in Medicine and Biology* 25(3), 463–479 (1980)
- [5] Boyd, S., Parikh, N., Chu, E., Peleato, B., Eckstein, J.: Distributed optimization and statistical learning via the alternating direction method of multipliers. *Found. Trends Mach. Learn.* 3(1), 1–122 (2011)
- [6] Bürger, B., Bettinghausen, S., M., R., Hesser, J.: Real-time gpu-based ultrasound simulation using deformable mesh models. *Transactions on Medical Imaging* 32(3), 609–618 (2013)
- [7] Chen, Z., Basarab, A., Kouame, D.: Compressive deconvolution in medical ultrasound imaging. *IEEE TMI* 35(3), 728–737 (2016)
- [8] Dantas, R.G., Costa, E.T., Leeman, S.: Ultrasound speckle and equivalent scatterers. *Ultrasonics* 43(6), 405–420 (2005)
- [9] Fish, D.A., Walker, J.G., Brinicombe, A.M., Pike, E.R.: Blind deconvolution by means of the richardson–lucy algorithm. *Journal of the Optical Society of America A* 12(1), 58–65 (Jan 1995)
- [10] Gao, H., Choi, H., Claus, P., Boonen, S., Jaecques, S., Van Lenthe, G., Van der Perre, G., Lauriks, W., D’hooge, J.: A fast convolution-based methodology to simulate 2-D/3-D cardiac ultrasound images. *IEEE TUFFC* 56(2), 404–409 (2009)
- [11] Goksel, O., Salcudean, S.E.: B-mode ultrasound image simulation in deformable 3-D medium. *IEEE TMI* 28(11), 1657–69 (2009)
- [12] Gray, R.M.: Toeplitz and circulant matrices: A review. *Communications and Information Theory* 2(3), 155–239 (Aug 2005)
- [13] Hasan, M.K., Rabbi, M.S.E., Lee, S.Y.: Blind deconvolution of ultrasound images using l_1 -norm-constrained block-based damped variable step-size multichannel lms algorithm. *IEEE TUFFC* 63(8), 1116–1130 (2016)
- [14] Huber, P.J.: Robust regression: asymptotics, conjectures and monte carlo. *The Annals of Statistics* pp. 799–821 (1973)
- [15] Hundt, E.E., Trautenberg, E.A.: Digital processing of ultrasonic data by deconvolution. *IEEE Transactions on Sonics and Ultrasonics* 27(5), 249–252 (1980)
- [16] Ilyina, N., Hermans, J., Verboven, E., Abeele, K.V.D., D’Agostino, E., D’hooge, J.: Iterative reconstruction of the ultrasound attenuation coefficient from backscattered signals. *The Journal of the Acoustical Society of America* 137(4), 2424–2424 (2015)
- [17] Jensen, J.: Simulation of advanced ultrasound systems using Field II. In: *Proc. of ISBI*. pp. 636–639 (2004)
- [18] Jensen, J., Leeman, S.: Nonparametric estimation of ultrasound pulses. *IEEE Transactions on Biomedical Engineering* 41(10), 929–936 (1994)
- [19] Jirik, R., Taxt, T.: Two-dimensional blind bayesian deconvolution of medical ultrasound images. *IEEE TUFFC* 55(10), 2140–2153 (2008)
- [20] Mattausch, O., Goksel, O.: Scatterer reconstruction and parametrization of homogeneous tissue for ultrasound image simulation. In: *Proceedings IEEE EMBC*. pp. 6350–6353 (Aug 2015)
- [21] Mattausch, O., Goksel, O.: Image-based PSF estimation for ultrasound training simulation. In: *Workshop on Simulation and Synthesis in Medical Imaging (SAHSIMI)* (Oct 2016)
- [22] Mattausch, O., Goksel, O.: Monte-carlo ray tracing for realistic ultrasound training simulation. In: *Eurographics Workshop on Visual Computing for Biology and Medicine* (Oct 2016)
- [23] Mattausch, O., Maxim, M., Goksel, O.: Realistic ultrasound simulation of complex surface models using interactive monte-carlo path tracing. *Computer Graphics Forum* (2017)
- [24] Mattausch, O., Ren, E., Bajka, M., Vanhoey, K., Goksel, O.: Comparison of texture synthesis methods for content generation in ultrasound simulation for training. In: *Proceedings SPIE*. vol. 10135, pp. 10135 – 10135 – 10 (2017)
- [25] Meunier, J., Bertrand, M., Mailloux, G.: A model for dynamic texture analysis in two-dimensional echocardiograms of the myocardium. *SPIE* 0768, 193–200 (1987)
- [26] Michailovich, O.V., Tannenbaum, A.: Blind deconvolution of medical ultrasound images: A parametric inverse filtering approach. *IEEE Transactions on Image Processing* 16(12), 3005–3019 (2007)
- [27] Ng, J., Prager, R., Kingsbury, N., Treece, G., Gee, A.: Wavelet restoration of medical pulse-echo ultrasound images in an em framework. *IEEE TUFFC* 54(3), 550–568 (2007)
- [28] Oosterveld, B., Thijssen, J., Verhoef, W.: Texture of B-mode echograms: 3-D simulations and experiments of the effects of diffraction and scatterer density. *Ultrasonic Imaging* 7(2), 142–160 (1985)
- [29] Ozkan, E., Tanner, C., Kastelic, M., Mattausch, O., Makhinya, M., Goksel, O.: Robust motion tracking in liver from 2d ultrasound images using supporters. *International Journal of Computer Assisted Radiology and Surgery* 12(6), 941–950 (2017)
- [30] Reis, G., Lappe, B., Kohn, S., Weber, C., Bertram, M., Hagen, H.: Towards a virtual echocardiographic tutoring system. In: *Visualization in Medicine and Life Sciences*, pp. 99–119. Springer Berlin (2008)
- [31] Sanabria, S.J., Goksel, O.: Hand-held sound-speed mammography based on ultrasound reflector tracking. In: *MICCAI*. pp. 568–576 (2016)
- [32] Scheipers, U.: Contemporary Interventional Ultrasonography in Urology, chap. *Ultrasonic Tissue Characterization*, pp. 143–177. Springer (2009)
- [33] Shin, H.C., Prager, R., Gomersall, H., Kingsbury, N., Treece, G., Gee, A.: *Acoustical Imaging: Volume 30*, chap. *Medical Ultrasound Image Deconvolution*, pp. 371–378. Springer Netherlands (2011)
- [34] Tanner, C., Flach, B., Eggenberger, C., Mattausch, O., Bajka, M., Goksel, O.: 4D Reconstruction of Fetal Heart Ultrasound Images in Presence of Fetal Motion, pp. 593–601. Springer International Publishing (2016)
- [35] Tanner, C., Flach, B., Eggenberger, C., Mattausch, O., Bajka, M., Goksel, O.: Consistent reconstruction of 4d fetal heart ultrasound images to cope with fetal motion. *International Journal of Computer Assisted Radiology and Surgery* (2017)
- [36] Taxt, T.: Restoration of medical ultrasound images using two-dimensional homomorphic deconvolution. *IEEE TUFFC* 42(4), 543–554 (1995)
- [37] Taxt, T.: Three-dimensional blind deconvolution of ultrasound images. *IEEE TUFFC* 48(4), 867–871 (2001)
- [38] Taxt, T.: Comparison of cepstrum based methods for radial blind deconvolution of ultrasound images. *IEEE TUFFC* 1417(44), 666–674 (1997)
- [39] Wagner, R., Smith, S., Sandrik, J., Lopez, H.: Statistics of speckle in ultrasound b-scans. *IEEE Transactions on Sonics and Ultrasonics* 30(3), 156–163 (1983)
- [40] Wang, L., Gordon, M., Zhu, J.: Regularized least absolute deviations regression and an efficient algorithm for parameter tuning. In: *Proceedings Conference on Data Mining*. pp. 690–700 (2006)
- [41] Wang, Z., Bovik, A.C., Sheikh, H.R., Simoncelli, E.P.: Image quality assessment: From error visibility to structural similarity. *IEEE Transactions on Image Processing* 13(4), 600–612 (2004)
- [42] Wein, W., Brunke, S., Khamene, A., Callstrom, M., Navab, N.: Automatic CT-ultrasound registration for diagnostic imaging and image-guided intervention. *Medical Image Analysis* 12(5), 577–585 (2008)
- [43] Yang, J., Zhang, Y.: Alternating direction algorithms for l_1 -problems in compressive sensing. *SIAM Journal on Scientific Computing* 33(1), 250–278 (2011)
- [44] Zhao, N., Basarab, A., Kouame, D., Tourneret, J.Y.: Joint segmentation and deconvolution of ultrasound images using a hierarchical bayesian model based on generalized gaussian priors. *IEEE Transactions on Image Processing* 25(8), 3736–3750 (2016)